

## **Supplementary Information**

### **Multifunctional biophotonic nanostructures inspired by longtail glasswing butterfly for medical devices**

Vinayak Narasimhan<sup>†</sup>, Radwanul Hasan Siddique<sup>†</sup>, Jeong Oen Lee, Shailabh Kumar, Blaise Ndjamen, Juan Du, Natalie Hong, David Sretavan<sup>\*</sup>, and Hyuck Choo<sup>\*</sup>

<sup>†</sup>These authors contributed equally to this work.

<sup>\*</sup>These authors are co-corresponding authors.

<sup>\*</sup>E-mail: [hchoo@caltech.edu](mailto:hchoo@caltech.edu), [David.Sretavan@ucsf.edu](mailto:David.Sretavan@ucsf.edu)

## Supplementary Section SII | Biophotonic nanostructures on *C. faunus* butterfly wings

Numerous living organisms possess fascinating structural coloration. However, transparency in insects is rare to observe among terrestrial life due to significant surface reflections between living tissues and air<sup>1,2</sup>. In this context, the longtail glasswing *C. faunus* butterfly is an interesting example given it possesses the structural basis to support both reflection-based coloration and transmission-based transparency. The transparency of the postdiscal area can be well-explained by effective medium theory and a transfer matrix model similar to other anti-reflective subwavelength nanostructures found in nature considering low absorption of chitin<sup>2,3</sup>. The subwavelength nanodome-shaped structures of the postdiscal area induces a refractive index with a linear gradient from 1 for air to 1.56 for the chitin membrane, and effectively reduces surface reflection<sup>2,3</sup>. Nanodome-shaped structures of the postdiscal area are hexagonally arranged and hence, a hexagonal unit cell was considered with an area of  $A_{\text{hex}} = \sqrt{3}/2d^2$  where  $d$  is the center-to-center distance between adjacent nanodomains. The radius of the nanodome at height  $z$  was provided by  $r(z) = r_0 \sqrt{(1 - z/h)}$ , where  $h$  is the height of the nanodomains, and  $r_0$  is the base radius that is equal to  $d/2$ . Consequently, the postdiscal nanodome area at height  $z$  is given by  $A_{\text{TP}}(z) = \pi r_0^2 (1 - z/h)$ , and the volume fraction of chitin as a function of actual height is given by:

$$f_{\text{TP}} = \begin{cases} 1 & \text{for } z < 0 \\ \frac{\pi}{2\sqrt{3}} \left(1 - \frac{z}{h}\right) & \text{for } 0 \leq z \leq h \\ 0 & \text{for } z > h \end{cases} \quad (1)$$

The base of the nanodomains was defined to include the origin of the  $z$ -axis at its centre. The remaining fraction of air is given by  $f_{\text{air}} = 1 - f_{\text{TP}}$ . After determining the volume fraction, the effective refractive index was calculated for any  $z$  using the well-known Maxwell-Garnett model. Then, the optical admittance and the corresponding reflection ( $R$ ) and transmission ( $T$ ) spectra of the stacked thin layers were calculated using a characteristic matrix method<sup>3</sup>.

The nanostructures of the basal area, however, utilize a different physics to remain optically transparent in the visible spectrum. The transparency occurs due to non-resonant forward Mie scattering from low index chitin ( $n = 1.56$ )<sup>4</sup> nanostructures that can be calculated by rigorously solving the Maxwell's equations<sup>5,6</sup> (See Fig. 2f). Finite-difference time-domain (FDTD) simulations were performed using a commercial FDTD software (Lumerical Solutions Inc.) to numerically calculate the reflection ( $R$ ) and transmission ( $T$ ) of the basal area.

In order to compare the simulated transmission spectra of postdiscal and basal areas with experimental spectra, the membrane absorption and light reflections from its backside were considered assuming the wing membrane was surrounded by nanostructures on both sides. Considering the thickness of the wing membrane  $l$  (500 nm) and absorption coefficient  $\alpha$  ( $\alpha = 4\pi\kappa/\lambda$

where  $\kappa = 0.008 \pm 0.001$ , the extinction coefficient considered here for the chitin), the final transmittance ( $T_F$ ) can be calculated by<sup>2</sup>:

$$T_F = \frac{T^2 e^{-\alpha l}}{1 - R^2 e^{-2\alpha l}}. \quad (2)$$

The simulated transmission spectra of both postdiscal and basal areas were plotted in Supplementary Fig. S2 along with the experimental outcomes, showing good agreement.

The angle-independent scattering properties of the basal area as found in Fig. 2j are directly correlated to the isotropic spatial frequency of the short-range-ordered nanostructures. For example, if we consider light with an incident wave vector  $\mathbf{k}_i$  being scattered to a wave vector  $\mathbf{k}_s$ , the difference between  $\mathbf{k}_i$  and  $\mathbf{k}_s$  can be provided by the spatial frequency  $\mathbf{k}_b$  of the structure, i.e.  $\mathbf{k}_s - \mathbf{k}_i = \mathbf{k}_b$ <sup>7</sup>. Due to the isotropic nature of the spatial frequency  $\mathbf{k}_b$  (see the FFT diagram in Fig. 2D in the main manuscript), the  $\mathbf{k}_s - \mathbf{k}_i$  will remain the same irrespective of the incident angle, thereby improving the angle-independent scattering properties.

To elucidate the biological significance of the dual nano-structural basis for transparency of the *C. faunus* wing, we illuminated the wings under ultraviolet (UV) light and captured images using a camera (Supplementary Fig. S3). No UV signature in the postdiscal areas was observed, whereas the basal areas showed violet-coloured reflectance under UV illumination (Supplementary Fig. S3). The short-range-ordered nanostructures with subwavelength periods in the postdiscal areas exhibited minimal scattering and high transparency in the UV-VIS light. However, similar nanostructures in the basal areas with larger inter-structural spacing comparable to the light wavelength generated backscattering in the UV range. The short-range order of the nanostructures in the spatial arrangement introduces a phase correlation in the backscattered light, leading to a coherent reflection peak in the UV regime as shown in Supplementary Fig. S4A. The characteristic length scale of the nanostructures generates such strong backward scattering of light within a narrow frequency range<sup>8</sup>. In general, for any wave vector of  $\mathbf{k} > \mathbf{k}_b/2$ , short-range structural order introduces a phase correlation of light scattered by adjacent particles<sup>9</sup>.  $\mathbf{k}_b$  ranges between  $0.021 \text{ nm}^{-1}$  and  $0.032 \text{ nm}^{-1}$  in our 2D FFT calculation of the basal area and hence  $\mathbf{k}_b/2$  corresponds to the frequencies in the blue spectrum. Therefore, coherent backscattered peak should appear in the frequencies higher than the blue spectrum, i. e. in the UV regime, which agrees with our experimental outcome.

Butterflies are known to use the UV regime as a key spectral range for mating signals<sup>11-13</sup>, and the nanostructures with larger spacing in the basal area may play an important role in this regard. The UV signature with a peak at a wavelength of 345 nm is confirmed by the optical spectra shown in Supplementary Fig. S4A of the basal area. The total reflection of postdiscal area is remarkably low over the whole UV-VIS regime. In order to confirm that the UV reflection of the basal area is structure-based, we removed the structural effect by soaking the wing in bromoform ( $n = 1.57$ ) to match the refractive index of the inter-structural space to that of the nanostructures. After soaking, we

repeated the reflection measurement and observed no reflection from the basal region confirming the structural origin of the reflection property (Supplementary Fig. S4B).

Therefore, the short-range-ordered nanostructures on the *C. faunus* wings produce dual optical functionality – transparency in the visible range and reflectance in the UV regime - that assists in camouflaging<sup>1,14</sup> and mating<sup>11–13</sup> while keeping the wings sterile by resisting microbial growth (Figs. S5 and S6).

## **Supplementary Section SI2 | Aspect-ratio optimization of the nanostructured on the Si<sub>3</sub>N<sub>4</sub> surface**

As mentioned in the manuscript, an antifouling approach relying on physical lysis may damage tissues and cells that come in contact with the implant, which may not be suitable for some medical uses. The aspect-ratio of the nanostructures was kept below 1 to rely on the hydrophilicity of the nanostructured Si<sub>3</sub>N<sub>4</sub> surfaces to promote antifouling through anti-adhesion instead of through physical lysis. A literature survey on this phenomenon is summarized in Table S1, revealing the aspect-ratio of 1 or greater will cause physically induced lysis on both naturally occurring and synthetic nanostructured surfaces.

With this background in mind, the nanostructure topography was optimized to an average aspect-ratio of 0.45 and a flat disk-shaped top. This aspect-ratio was chosen because there was no significant statistical difference in the anti-adhesion properties between nanostructured Si<sub>3</sub>N<sub>4</sub> surfaces with an aspect-ratio of 0.45 and those with an aspect-ratio ranging from 0.45 to 0.9 (Supplementary Fig. S7, S11 and S16).

Furthermore, optical simulations indicate that increasing the aspect-ratio broadens the resonance peak of the nanostructured Si<sub>3</sub>N<sub>4</sub> (Supplementary Fig. S10). The flat Si<sub>3</sub>N<sub>4</sub>-membrane produces a ballistic (specular) transmission peak due to the phase delay introduced by the thin membrane that causes light interference. The integration of nanostructures on the Si<sub>3</sub>N<sub>4</sub>-membrane broadens the total transmission-peak profile due to the combination of ballistic (due to the thin membrane) and scattered transmission (due to the nanostructures)<sup>15</sup>.

## **Supplementary Section SI3 | Anti-biofouling properties of the nanostructured Si<sub>3</sub>N<sub>4</sub> surface**

We describe in this section our findings on the improved biocompatibility of the nanostructures: the nanostructures resist protein adhesion as well as prokaryotic and mammalian eukaryotic biofouling due to the surface hydrophilicity and nanostructured topology. To reach our conclusion, we have performed extensive literature study on the mechanisms behind the adhesion of plasma proteins, prokaryotes, and eukaryotes on the surface of implanted biomaterials; and also carried out a comprehensive set of experimental measurements and theoretical analysis performed on the nanostructured surfaces.

The adsorption behaviour of a protein onto a surface is a complex process, which is influenced by the nature of the protein as well as the properties of the surface, and it may involve several steps such as protein association-disassociation, change in conformation, denaturation, and charge interaction between neighbouring proteins<sup>16–18</sup>. As a result, there is a huge variation among underlying anti-biofouling mechanisms and resulting outcomes of surfaces that have been proposed to control biofouling<sup>19–21</sup>. In the case of the nanostructured Si<sub>3</sub>N<sub>4</sub> surface presented in this manuscript, our results indicate that the high degree of wettability (or hydrophilicity) acts in concert with the nanostructured surface topology to produce improved biocompatibility. We discuss this behaviour of the substrate by considering energy barriers in the following paragraphs.

Let us consider attachment of a protein to a surface first. The reaction can be represented as:



Where, protein molecules in an aqueous media or liquid (PL) are interacting with a surface submerged in liquid (SL) and leading to adsorption of protein molecules on the surface represented as PS. The effective free energy change for this reaction can be represented as  $\Delta G_{PS}$ , which is dependent on the interfacial free energies of protein-liquid ( $\gamma_{PL}$ ), protein-surface ( $\gamma_{PS}$ ), and surface-liquid ( $\gamma_{SL}$ )<sup>22</sup>. This can be shown as<sup>23</sup>:

$$\Delta G_{PS} = \gamma_{PS} - (\gamma_{PL} + \gamma_{SL}) \quad (4)$$

For improved biocompatibility and reduced adsorption, the net energy change for the process should be positive, i.e.  $\Delta G_{PS} > 0$ , and a higher value of  $\Delta G_{PS}$  would imply an unstable protein-surface interaction or a higher resistance to biofouling due to easy detachment. The interfacial free energies are dependent on the interactions between (1) the substrate surface and the liquid media (governed by the wettability of the surface); (2) the protein molecules and the liquid media (governed by the structure and distribution of hydrophobic/hydrophilic residues on the proteins); and (3) the protein molecules and the surface (dependent on both of the above factors). Normally proteins hide their hydrophobic residues away from water while their charged, polar amino-acid side-chains are exposed to water<sup>24,25</sup>. As a result, charges on the proteins will also influence protein-protein interactions, which can lead to an aggregation of proteins in solution.

Noticeably hydrophilic surfaces such as nanostructures improve the affiliation between the surface and water molecules by lowering  $\gamma_{SL}$ , which is favourable for improved biocompatibility. If the protein has a higher degree of hydrophobic residues or behaviour,  $\gamma_{PS}$  will be higher, which is favourable, but  $\gamma_{PL}$  will also be higher, which is unfavourable. Decrease in hydrophobicity of the protein will result in both lowering the  $\gamma_{PS}$  (unfavourable) and  $\gamma_{PL}$  (favourable). Changes in protein conformation during the surface adsorption process can also occur<sup>16,17</sup>, changing the interfacial free energy ( $\gamma_{PS}$ ).

The surface-energy analysis indicates that in the case of the nanostructured Si<sub>3</sub>N<sub>4</sub> surface, the increased hydrophilicity of the substrate also increases the energy barrier for protein adsorption on the surface. That is to say, there is a larger energy barrier to the replacement of water molecules in contact with the nanostructured Si<sub>3</sub>N<sub>4</sub> surface (measured contact angle: 17°) with proteins as compared to a mildly hydrophilic surface such as flat Si<sub>3</sub>N<sub>4</sub> (measured contact angle: 38°). However, it is important to keep in mind that the degree of resistance to protein adsorption also depends on factors such as the structure, sequence, and nature of resultant charges on the protein molecules.

Previously, hydrophilic surfaces, which effectively bind water molecules and prevent protein adsorption, have been utilized for improved biocompatibility previously such as immobilized PEG-based films<sup>26,27</sup> and self-assembled monolayers (SAMs)<sup>28,29</sup>. However, the protein resistance of these surfaces decay over time due to factors such as auto-oxidation resulting in the formation of more non-polar and less hydrophilic functional groups such as aldehydes and ethers<sup>30</sup>. Additionally, these surfaces are susceptible to physical defects and therefore are not suitable for long-term usage<sup>31,32</sup>. The noticeable hydrophilicity of the nanostructured Si<sub>3</sub>N<sub>4</sub> surface results from the physical topology of the surface and is expected to show much better long-term reliability than chemical coatings.

To isolate the contribution from the improved hydrophilicity to the deterrence of protein adhesion, we plasma-treated flat Si<sub>3</sub>N<sub>4</sub> surfaces (Supplementary Fig. S17A) and compared them with non-treated flat Si<sub>3</sub>N<sub>4</sub> surfaces. Decrease in protein adsorption as a function of increasing surface wettability becomes evident when comparing the results obtained for plasma treated and non-plasma treated substrates, as shown in Supplementary Fig. S17B. After 2 hours of incubation, the extent of protein adhesion on the plasma-treated Si<sub>3</sub>N<sub>4</sub> and nanostructured Si<sub>3</sub>N<sub>4</sub> surfaces are almost the same. This could be attributed to the dominance of the antifouling contribution from the hydrophilicity as the length-scale of the nanotopology of the nanostructured Si<sub>3</sub>N<sub>4</sub> surface is over an order of magnitude greater than the size of proteins, implying that the nanoscale geometry effect is possibly negligible. However, after 24 hours, the nanostructured Si<sub>3</sub>N<sub>4</sub> surface displays the lowest contact angle and the greatest resistance to protein adsorption while the nonpermanent plasma-treated surface loses its hydrophilicity and its contact angle returns back to a value close to that of a non-treated flat Si<sub>3</sub>N<sub>4</sub> surface (Supplementary Fig. S17A).

When considering the case of cellular adhesion to surfaces, we can consider the following reaction:



Where, cells in an aqueous media or liquid (CL) are interacting with a surface submerged in liquid (SL) and leading to adsorption of cellular molecules on the surface represented as CS. The free energy change can be expressed as:

$$\Delta G_{CS} = \gamma_{CS} - (\gamma_{CL} + \gamma_{SL}) \quad (6)$$

The effect of surface wettability on the free energies in this case is also very similar with proteins. Improved hydrophilicity of the surface implies that  $\gamma_{SL}$  will be lower, which increases the barrier for displacement of water molecules on the surface by cells and is favourable for improving biocompatibility. The degree of improvement will once again be dependent on the other two terms ( $\gamma_{CS}$  and  $\gamma_{CL}$ ), which are dependent on the nature of charges on the cells and their apparent hydrophilicity or hydrophobicity (discussed in further detail by Liu *et al.*)<sup>23</sup>. Indeed, it has been shown that increase in surface hydrophobicity (contact angle change from 15° to 100°) correlated directly with increase in surface adsorption of bacteria, algal spores, and eukaryotic cells<sup>33–36</sup>. Our results (Supplementary Fig. S17C-D) show that there is a significant decrease in cellular adhesion upon increasing the hydrophilicity of flat silicon nitride surfaces through plasma oxidation, which agrees with the surface wettability model.

The second important contribution towards improved biocompatibility for the nanostructured  $\text{Si}_3\text{N}_4$  surface originates from the nanostructured surface topology. Being in the same length-scale or more typically an order of magnitude smaller than cells, nanotopology plays a greater role in biofouling resistance against bacteria and mammalian cells (Supplementary Fig. S17C-D). Various reports have claimed that structured surfaces reduce biofouling as compared to flat substrates<sup>21,33,34</sup>. Two primary cases can be considered when cells are interacting with patterned substrates. The first case is when cells can elongate to increase their interaction with the surface and fill the gaps between nanostructures<sup>37</sup>. This cellular elongation directly leads to an increase in surface tension along the cell membrane and has been modelled by Pogodin *et al.* assuming a planar piece of membrane<sup>38</sup>. The increase in interfacial surface energy is described by<sup>38</sup>,

$$\Delta\gamma_{CS} = \int \frac{\varepsilon\eta_0 d\sigma}{(1 + \alpha(r))} \quad (7)$$

where  $\eta_0$  represents the surface density of adsorption sites on the membrane;  $\varepsilon$  represents energy gained per unit of adsorption site;  $\alpha(r)$  represents the local degree of cell membrane stretching at point  $r$ ; and  $d\sigma$  is the elemental surface area. The integration is performed over the total contact area between the cell membrane and the nanostructured surface. For high-aspect-ratio structures such as the nanopillars (diameter 160 nm, height 200 nm) described by Pogodin *et al.*<sup>38</sup>, stretching of the membrane can eventually lead to rupture and cell lysis. For low-aspect-ratio nanostructures structures with an average diameter of 345 nm and height of 150 nm, our experimental results have not shown any signs of cell lysis (Supplementary Fig. S14-16), indicating that while membrane elongation is likely increasing  $\gamma_{CS}$  in equation 6 and improving biocompatibility of the substrate, cell membranes are not rupturing.

The second possible case occurs when the cell membrane does not elongate to fill the gaps in the nanopatterned substrate. It has been shown that this situation leads to a reduction in adhesion points between the substrate and cells<sup>39</sup>, leading to poor adhesion of cells on patterned surfaces as compared

to a flat surface and consequently easier detachment. Therefore, nanotopology-driven outcomes such as membrane deformation or reduction in adhesion points contribute towards destabilizing the interaction between the cell membrane and substrate, improving resistance to cellular adsorption. Our results demonstrate that nanostructured Si<sub>3</sub>N<sub>4</sub> surface shows a drastic decrease in both prokaryotic and mammalian cellular adhesion as compared to a flat substrate (with or without plasma treatment) due to the increased contribution from the nanotopology (Supplementary Fig. S17C-D). This is evident from the fact that greater cell adhesion resistance is offered by the nanostructured Si<sub>3</sub>N<sub>4</sub> surface over the plasma-treated Si<sub>3</sub>N<sub>4</sub> surface of a similar contact angle.

To summarize, based on evidences found in literatures and results obtained from our experiments, we have analysed the underlying mechanism that produced the much improved biocompatibility of the nanostructured substrate: it is the combination of (a) much-improved, nanopattern-based, hydrophilicity that increases the energy barrier for protein and cellular adhesion on the substrate; and (b) nanostructured surface topology, which reduces the energy barrier for detachment of cells from the surface and destabilizes cellular adhesion to the substrate.

#### References for Supplementary Information

1. Johnsen, S. Hidden in plain sight: the ecology and physiology of organismal transparency. *Biol. Bull.* **201**, 301–18 (2001).
2. Siddique, R. H., Gomard, G. & Hölscher, H. The role of random nanostructures for the omnidirectional anti-reflection properties of the glasswing butterfly. *Nat. Commun.* **6**, 6909 (2015).
3. Raut, H. K., Ganesh, V. A., Nair, a. S. & Ramakrishna, S. Anti-reflective coatings: A critical, in-depth review. *Energy Environ. Sci.* **4**, 3779 (2011).
4. Vukusic, P., Sambles, J. R., Lawrence, C. R. & Wootton, R. J. Quantified interference and diffraction in single Morpho butterfly scales. *Proc. R. Soc. B Biol. Sci.* **266**, 1403–1411 (1999).
5. Van de Hulst, H. C. & Twersky, V. Light scattering by small particles. *Phys. Today* **10**, 28–30 (1957).
6. Khudiyev, T., Huseyinoglu, E. & Bayindir, M. Non-resonant Mie scattering: Emergent optical properties of core-shell polymer nanowires. *Sci. Rep.* **4**, 4607 (2014).
7. Noh, H. *et al.* How Noniridescent Colors Are Generated by Quasi-ordered Structures of Bird Feathers. *Adv. Mater.* **22**, 2871–2880 (2010).
8. Prum, R. O., Torres, R. H., Williamson, S. & Dyck, J. Coherent light scattering by blue feather barbs. *Nature* **396**, 28–29 (1998).
9. Liew, S. F. *et al.* Short-range order and near-field effects on optical scattering and structural



- coloration. *Opt. Express* **19**, 8208–8217 (2011).
10. Saranathan, V. *et al.* Structure, function, and self-assembly of single network gyroid (I4132) photonic crystals in butterfly wing scales. *Proc. Natl. Acad. Sci.* **107**, 11676–11681 (2010).
  11. Papke, R. S., Kemp, D. J. & Rutowski, R. L. Multimodal signalling: structural ultraviolet reflectance predicts male mating success better than pheromones in the butterfly *Colias eurytheme* L.(Pieridae). *Anim. Behav.* **73**, 47–54 (2007).
  12. Kemp, D. J. Female mating biases for bright ultraviolet iridescence in the butterfly *Eurema hecabe* (Pieridae). *Behav. Ecol.* **19**, 1–8 (2007).
  13. Dushkina, N., Erten, S. & Lakhtakia, A. Coloration and Structure of the Wings of *Chorinea sylphina* Bates. *J. Lepid. Soc.* **71**, 1–11 (2017).
  14. Henderson, C. L. *Field Guide to the Wildlife of Costa Rica*. (University of Texas Press, 2002). at <<http://books.google.de/books?id=q2KzTTBMrLkC>>
  15. Limonov, M. F. & Richard, M. *Optical properties of photonic structures: interplay of order and disorder*. (CRC press, 2012).
  16. Buijs, J. & Hlady, V. Adsorption kinetics, conformation, and mobility of the growth hormone and lysozyme on solid surfaces, studied with TIRF. *J. Colloid Interface Sci.* **190**, 171–181 (1997).
  17. Roach, P., Farrar, D. & Perry, C. C. Interpretation of protein adsorption: surface-induced conformational changes. *J. Am. Chem. Soc.* **127**, 8168–8173 (2005).
  18. Wertz, C. F. & Santore, M. M. Adsorption and relaxation kinetics of albumin and fibrinogen on hydrophobic surfaces: single-species and competitive behavior. *Langmuir* **15**, 8884–8894 (1999).
  19. Genzer, J. & Efimenko, K. Recent developments in superhydrophobic surfaces and their relevance to marine fouling: a review. *Biofouling* **22**, 339–60 (2006).
  20. Xu, L.-C. & Siedlecki, C. A. Effects of surface wettability and contact time on protein adhesion to biomaterial surfaces. *Biomaterials* **28**, 3273–3283 (2007).
  21. Carman, M. L. *et al.* Engineered antifouling microtopographies—correlating wettability with cell attachment. *Biofouling* **22**, 11–21 (2006).
  22. Morra, M. *Water in biomaterials surface science*. (John Wiley & Sons, 2001).
  23. Liu, Y. *et al.* The influence of cell and substratum surface hydrophobicities on microbial attachment. *J. Biotechnol.* **110**, 251–256 (2004).
  24. Rose, G. D., Geselowitz, A. R., Lesser, G. J., Lee, R. H. & Zehfus, M. H. Hydrophobicity of

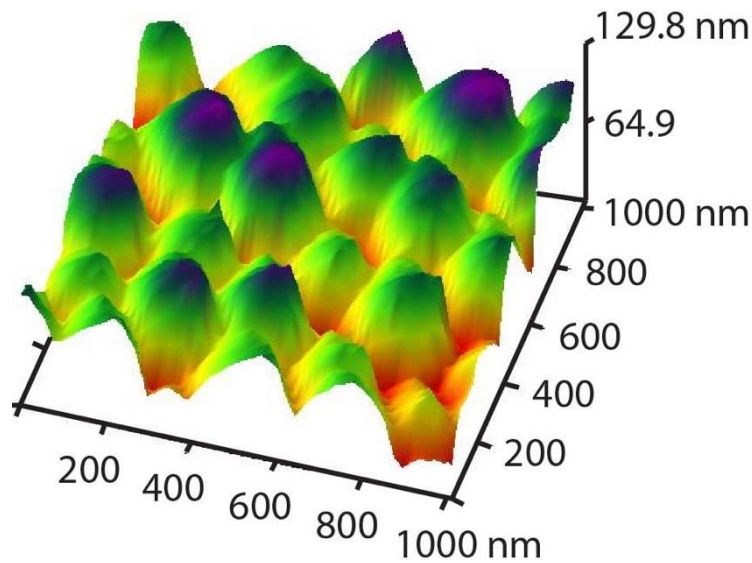
- amino acid residues in globular proteins. *Science* (80-. ). **229**, 834–839 (1985).
25. Dill, K. A. Dominant forces in protein folding. *Biochemistry* **29**, 7133–7155 (1990).
  26. Xia, N., May, C. J., McArthur, S. L. & Castner, D. G. Time-of-Flight Secondary Ion Mass Spectrometry Analysis of Conformational Changes in Adsorbed Protein Films. *Langmuir* **18**, 4090–4097 (2002).
  27. Bearinger, J. P. *et al.* Chemisorbed poly(propylene sulphide)-based copolymers resist biomolecular interactions. *Nat Mater* **2**, 259–264 (2003).
  28. Prime, K. L. & Whitesides, G. M. Self-assembled organic monolayers: model systems for studying adsorption of proteins at surfaces. *Science* (80-. ). **252**, 1164 LP-1167 (1991).
  29. Prime, K. L. & Whitesides, G. M. Adsorption of proteins onto surfaces containing end-attached oligo(ethylene oxide): a model system using self-assembled monolayers. *J. Am. Chem. Soc.* **115**, 10714–10721 (1993).
  30. Hucknall, A., Rangarajan, S. & Chilkoti, A. In Pursuit of Zero: Polymer Brushes that Resist the Adsorption of Proteins. *Adv. Mater.* **21**, 2441–2446 (2009).
  31. Banerjee, I., Pangule, R. C. & Kane, R. S. Antifouling Coatings: Recent Developments in the Design of Surfaces That Prevent Fouling by Proteins, Bacteria, and Marine Organisms. *Adv. Mater.* **23**, 690–718 (2011).
  32. Ma, H., Hyun, J., Stiller, P. & Chilkoti, A. ‘Non-Fouling’ Oligo(ethylene glycol)-Functionalized Polymer Brushes Synthesized by Surface-Initiated Atom Transfer Radical Polymerization. *Adv. Mater.* **16**, 338–341 (2004).
  33. Callow, M. E. *et al.* Use of self-assembled monolayers of different wettabilities to study surface selection and primary adhesion processes of green algal (Enteromorpha) zoospores. *Appl. Environ. Microbiol.* **66**, 3249–3254 (2000).
  34. Wiencek, K. M. & Fletcher, M. Bacterial adhesion to hydroxyl- and methyl-terminated alkanethiol self-assembled monolayers. *J. Bacteriol.* **177**, 1959–1966 (1995).
  35. Lee, J. H. & Lee, H. B. A wettability gradient as a tool to study protein adsorption and cell adhesion on polymer surfaces. *J. Biomater. Sci. Polym. Ed.* **4**, 467–481 (1993).
  36. Lee, J. H., Lee, S. J., Khang, G. & Lee, H. B. The Effect of Fluid Shear Stress on Endothelial Cell Adhesiveness to Polymer Surfaces with Wettability Gradient. *J. Colloid Interface Sci.* **230**, 84–90 (2000).
  37. Kooten, T. G. Van & Recum, A. F. Von. Cell adhesion to textured silicone surfaces: the influence of time of adhesion and texture on focal contact and fibronectin fibril formation. *Tissue Eng.* **5**, 223–240 (1999).

38. Pogodin, S. *et al.* Biophysical Model of Bacterial Cell Interactions with Nanopatterned Cicada Wing Surfaces. *Biophys. J.* **104**, 835–840 (2013).
39. Arnold, M. *et al.* Activation of integrin function by nanopatterned adhesive interfaces. *ChemPhysChem* **5**, 383–388 (2004).
40. Kim, S. *et al.* Nanostructured Multifunctional Surface with Antireflective and Antimicrobial Characteristics. *ACS Appl. Mater. Interfaces* **7**, 326–331 (2015).
41. Liu, L., Ercan, B., Sun, L., Ziemer, K. S. & Webster, T. J. Understanding the Role of Polymer Surface Nanoscale Topography on Inhibiting Bacteria Adhesion and Growth. *ACS Biomater. Sci. Eng.* **2**, 122–130 (2016).
42. Dickson, M. N., Liang, E. I., Rodriguez, L. A., Vollereaux, N. & Yee, A. F. Nanopatterned polymer surfaces with bactericidal properties. *Biointerphases* **10**, 21010 (2015).
43. Sengstock, C. *et al.* Structure-related antibacterial activity of a titanium nanostructured surface fabricated by glancing angle sputter deposition. *Nanotechnology* **25**, 195101 (2014).
44. Ivanova, E. P. *et al.* Bactericidal activity of black silicon. *Nat. Commun.* **4**, 2838 (2013).
45. Pham, V. T. H. *et al.* ‘Race for the Surface’: Eukaryotic Cells Can Win. *ACS Appl. Mater. Interfaces* **8**, 22025–22031 (2016).
46. Kelleher, S. M. *et al.* Cicada Wing Surface Topography: An Investigation into the Bactericidal Properties of Nanostructural Features. *ACS Appl. Mater. Interfaces* **8**, 14966–14974 (2016).
47. Ivanova, E. P. *et al.* Natural Bactericidal Surfaces: Mechanical Rupture of *Pseudomonas aeruginosa* Cells by Cicada Wings. *Small* **8**, 2489–2494 (2012).

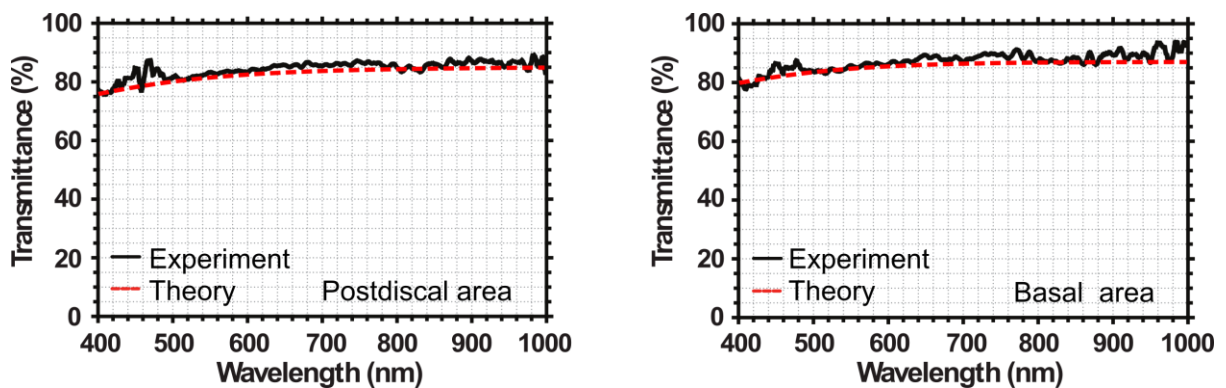
## Supplementary Figures and Tables

**Supplementary Table S1 | Summary of the literature survey on biophysical properties of synthetic and naturally occurring nanopillars.** Butterfly species and materials discussed or utilised in this work are highlighted and marked as \* in the comments section.

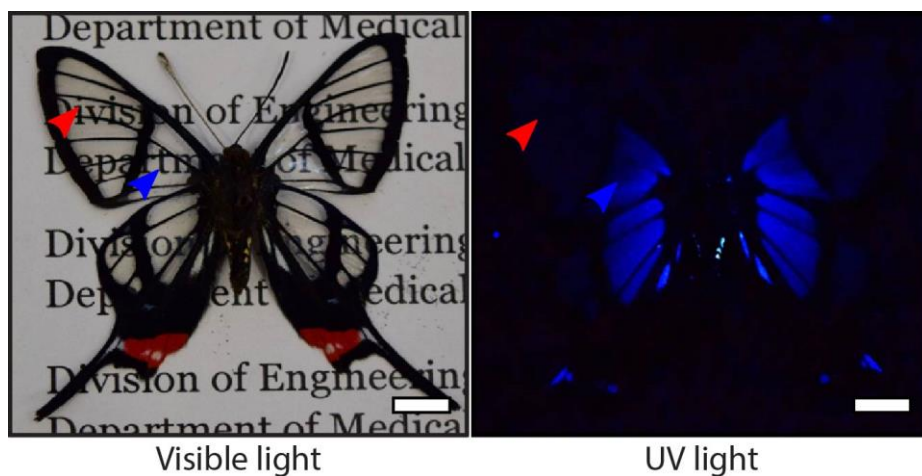
Structure Type	Material/Species	Aspect Ratio	Surface Wetting Properties		Cell Type Tested		Incubation Time		Comments
			Surface Type	Contact Angle (degrees)	Prokaryotes	Eukaryotes	Prokaryotes	Eukaryotes	
Synthetic	Silicon Nitride	0.15 - 0.9	Hydrophilic	22° - 13°	<i>E. coli</i>	<i>HeLa cells</i>	4 hrs	1, 2, 3 days	Sharp drop in prokaryote and adhesion with structuring*.
	PMMA	1.53	Hydrophobic	114°	<i>P. aeruginosa</i> , <i>E. coli</i>	<i>C2C12 myoblast</i>	4, 8 hrs	7 days	Fair bactericidal activity. However, eukaryotes killed <sup>40</sup> .
	PDMS	-	Hydrophilic	66.6°	<i>E. coli</i> , <i>S. aureus</i>	<i>Human fibroblasts</i> , <i>Endothelial cells</i>	1, 2 days	4 hrs	Considerable bactericidal activity. Proliferation of eukaryotes <sup>41</sup> .
	PMMA	1.39 - 3.0	Hydrophilic	-	<i>E. coli</i>	-	3, 18, 24 hrs	-	Adhesion density similar for all samples tested. Bactericidal activity increased with aspect ratio <sup>42</sup> .
	Titanium	3.0 - 4.0	Hydrophilic	41.4°	<i>E. coli</i> , <i>S. aureus</i>	<i>HMSC</i> , <i>PBMC</i>	1, 3 hrs	2 days	Bactericidal activity shown only against gram-negative <i>E. coli</i> . Additionally, proliferation of HMSC and PBMC observed <sup>43</sup> .
	Black Silicon	7.14 - 10.0	Hydrophilic	80°	<i>P. aeruginosa</i> , <i>S. aureus</i> , <i>B. subtilis</i>	<i>COS-7</i>	3, 18, 24, 30 hrs	1, 3, 7 days	Considerable bactericidal activity <sup>44,45</sup> . Proliferation of eukaryotes <sup>45</sup> .
Natural	<i>A. spectabilis</i>	0.88	Hydrophobic	95.65°	<i>P. fluorescens</i>	-	30 mins	-	Minimal bactericidal activity. No eukaryotes tested <sup>46</sup> .
	<i>C. faunus</i>	1	Hydrophobic	85.16° & 105.42°	<i>E. coli</i>	<i>HeLa cells</i>	4 hrs	1, 2, 3 days	Cell lysis and minimal cell adhesion in prokaryotes and eukaryotes*.
	<i>C. aguila</i>	1.15	Hydrophobic	113.2°	<i>P. fluorescens</i>	-	30 mins	-	Minimal bactericidal activity. No eukaryotes tested <sup>46</sup> .
	<i>M. intermedia</i>	1.55	Hydrophobic	135.5°	<i>P. fluorescens</i>	-	30 mins	-	Considerable bactericidal activity. No eukaryotes tested <sup>46</sup> .
	<i>P. claripennis</i>	2.0 - 3.33	Superhydrophobic	147° - 172°	<i>P. aeruginosa</i>	-	1 hr	-	Extensively studied. Considerable bactericidal activity. No eukaryotes tested <sup>38,47</sup> .
	<i>D. bipunctata</i>	2.67 - 8.0	Superhydrophobic	153°	<i>P. aeruginosa</i> , <i>S. aureus</i> , <i>B. subtilis</i>	-	3, 18, 24, 30 hrs	-	Considerable bactericidal activity. No eukaryotes tested <sup>44</sup> .



**Supplementary Figure S1 | Nanostructures in the basal area of the *C. faunus* wing.** 3D atomic force microscopy (AFM) image of the nanostructures found on the *C. faunus* wing.

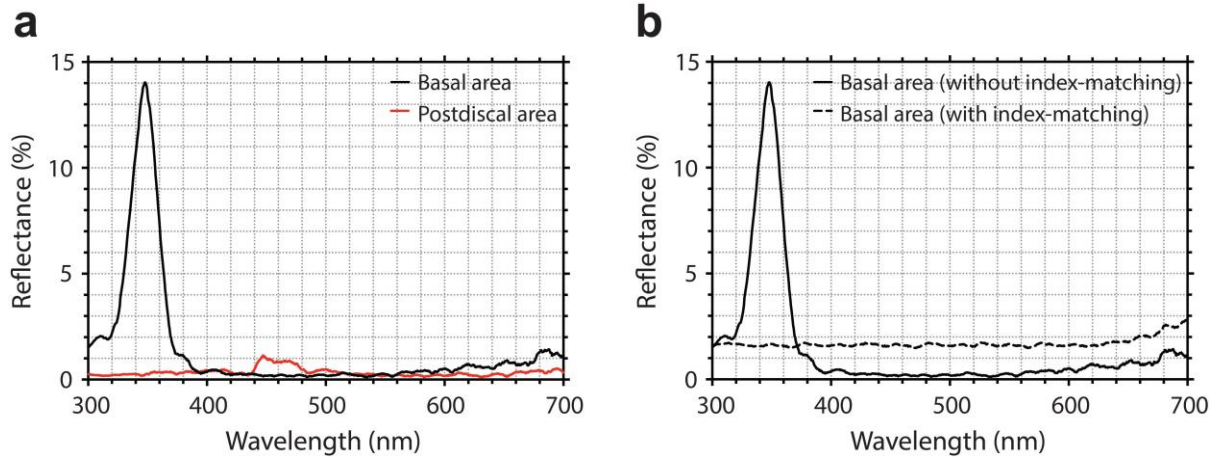


**Supplementary Figure S2 | Comparisons of simulated and experimentally measured total transmittance spectra of the postdiscal and basal areas.** Simulation results (see details in the supplementary section S11) are in accord with the experimental outcomes, confirming the discussed physics for the transparency observed in the *C. faunus* butterfly wings.

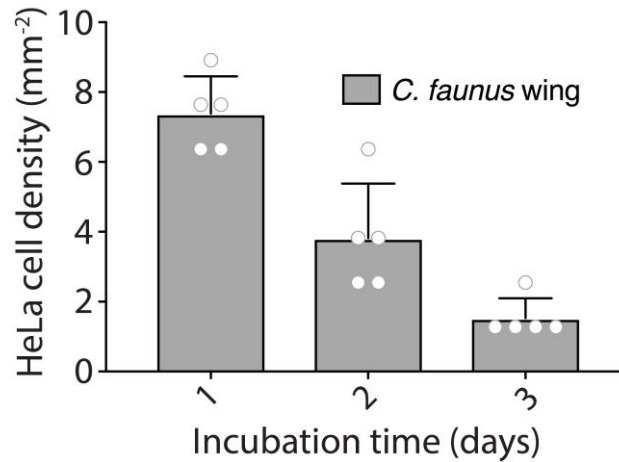


**Supplementary Figure S3 | *C. faunus* under visible and UV light.** Photos of a *C. faunus* butterfly under visible and UV light. The red and blue arrows indicate the postdiscal and basal areas,

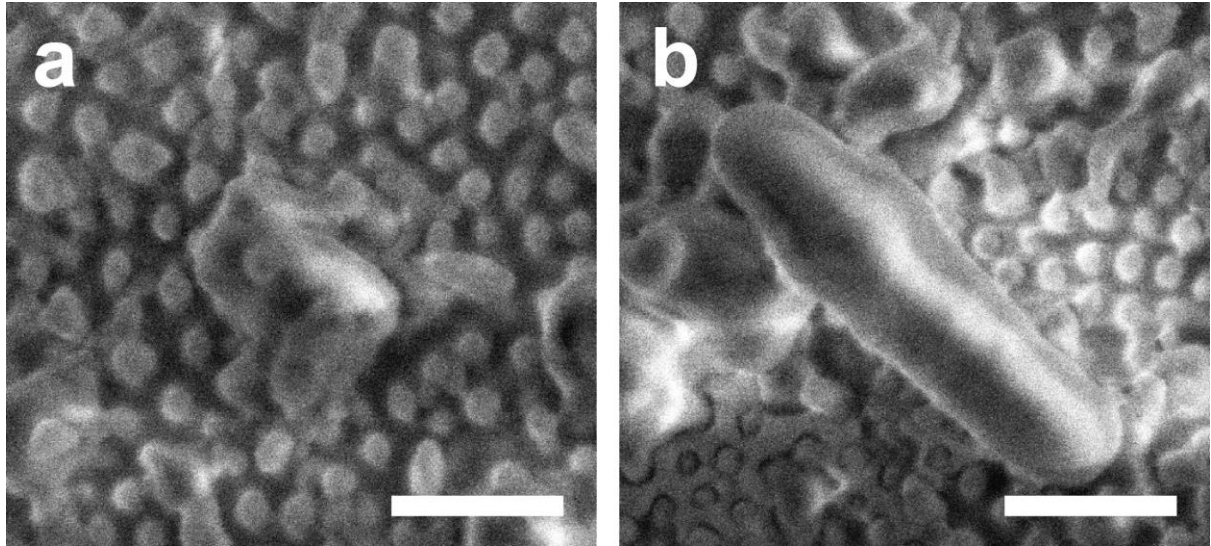
respectively. Scale bar: 1 cm.



**Supplementary Figure S4 | Reflection spectra of postdiscal and basal transparent areas of *C. faunus* wing.** **a**, The UV signature of the basal area is clearly visible while the reflection from the postdiscal area is negligible confirming the violet-coloured reflectance under UV illumination of the basal area as seen in Fig. 2a of the manuscript. **b**, The UV-VIS reflection spectra were obtained when soaking the wing in an index-matching liquid (bromoform,  $n = 1.57$ ) to cancel out the structural contribution. In this case, no reflectance was observed under UV illumination from the basal area confirming the structural origin of this unique UV signature.

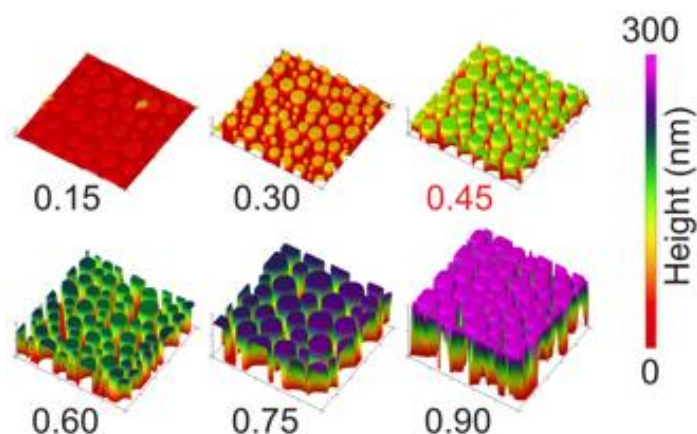


**Supplementary Figure S5 | Biophysical interaction between HeLa cells and the nanostructures on the *C. faunus* wing.** The nanostructures have an aspect-ratio of approximately 1. Cell densities decreased with increased incubation time, indicating disruption of cellular growth ( $n = 5$  representative images). The experiment was conducted once. Error bars are given by the standard deviation about the mean.

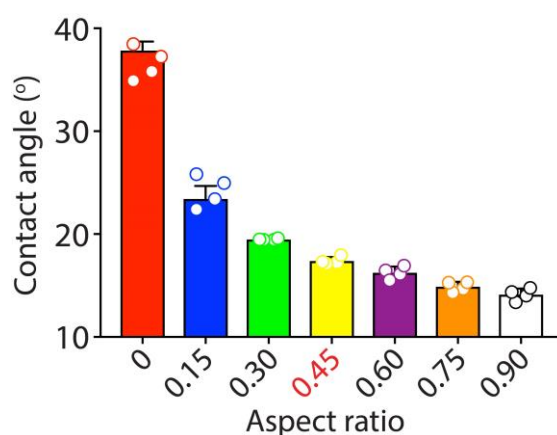


**Supplementary Figure S6 | Biophysical interaction between *E. coli* and the nanostructures on the *C. faunus* wing.** Several ( $n = 20$ ) high-resolution SEM images of *E. coli* on the nanostructures were observed. **a**, Close to 85% of the observed fields-of-view contained bacteria with significantly altered morphology indicating that the nanostructures disrupt bacterial shape and integrity possibly through localized stretching and stresses much like in high aspect ratio nanostructures reported in literature. **b**, The remaining 15% of the observed fields-of-view contained larger bacteria that maintained their shape despite marginal stretching clearly observed on their periphery. Scale 1  $\mu\text{m}$ .



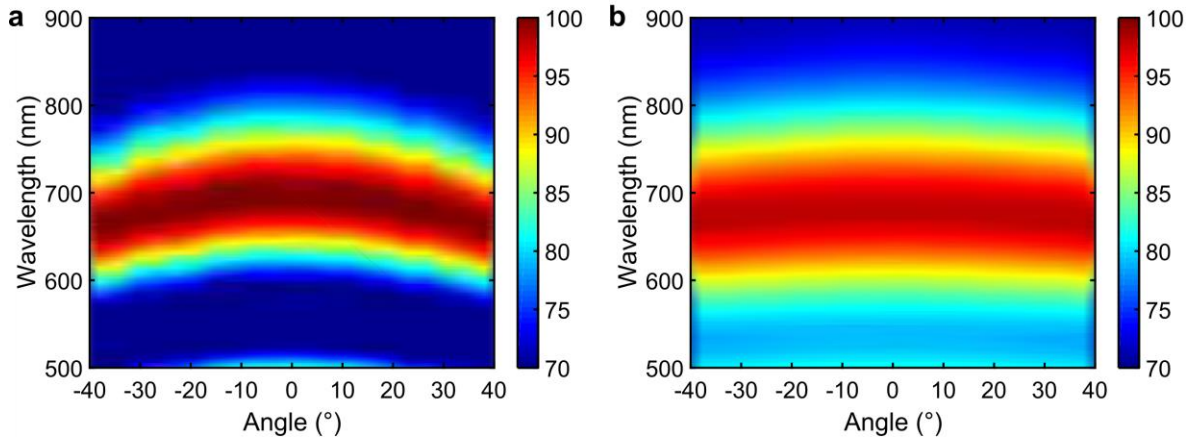


**Supplementary Figure S7 | Structural variation of the nanostructured  $\text{Si}_3\text{N}_4$ .** 3D atomic force microscopic images of nanostructured  $\text{Si}_3\text{N}_4$  templates with aspect-ratios ranging from 0.15 to 0.90. The aspect-ratio chosen for the nanostructured  $\text{Si}_3\text{N}_4$ -membrane and sensor is highlighted in red.

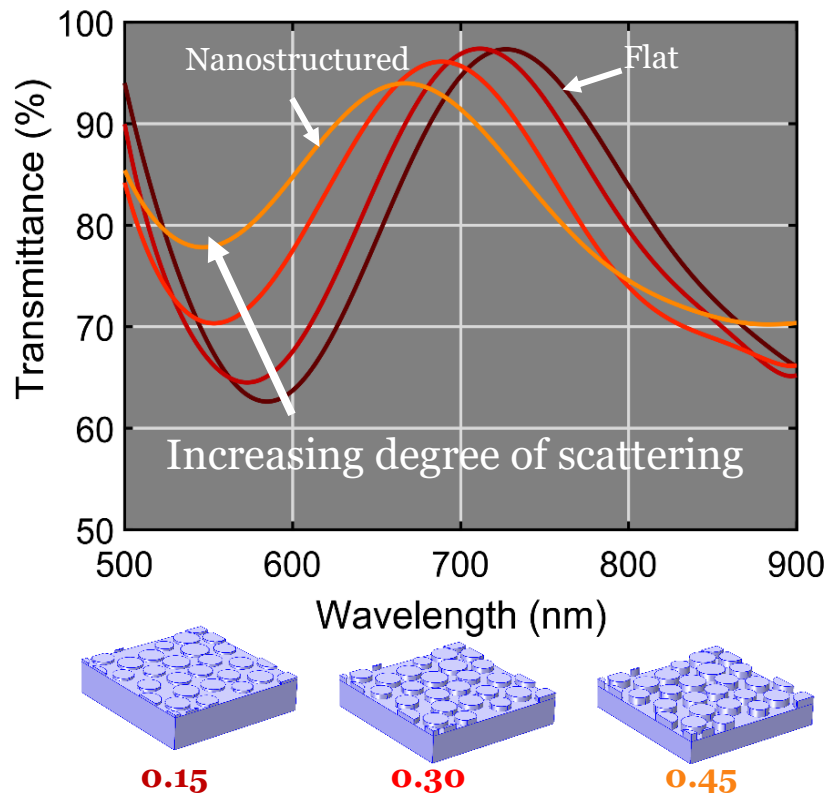


**Supplementary Figure S8 | Contact angle variation of the nanostructured  $\text{Si}_3\text{N}_4$ .** The wetting properties of nanostructured  $\text{Si}_3\text{N}_4$  templates with aspect-ratios ranging from 0.15 to 0.90 ( $n = 4$  measurements). Unmodified flat  $\text{Si}_3\text{N}_4$  (aspect-ratio = 0) is moderately hydrophilic. Through structuring, the hydrophobicity of nanostructured  $\text{Si}_3\text{N}_4$  increased. The aspect-ratio chosen for the nanostructured  $\text{Si}_3\text{N}_4$ -membrane and sensor is highlighted in red. The experiment was conducted once. Error bars are given by the standard deviation about the mean.

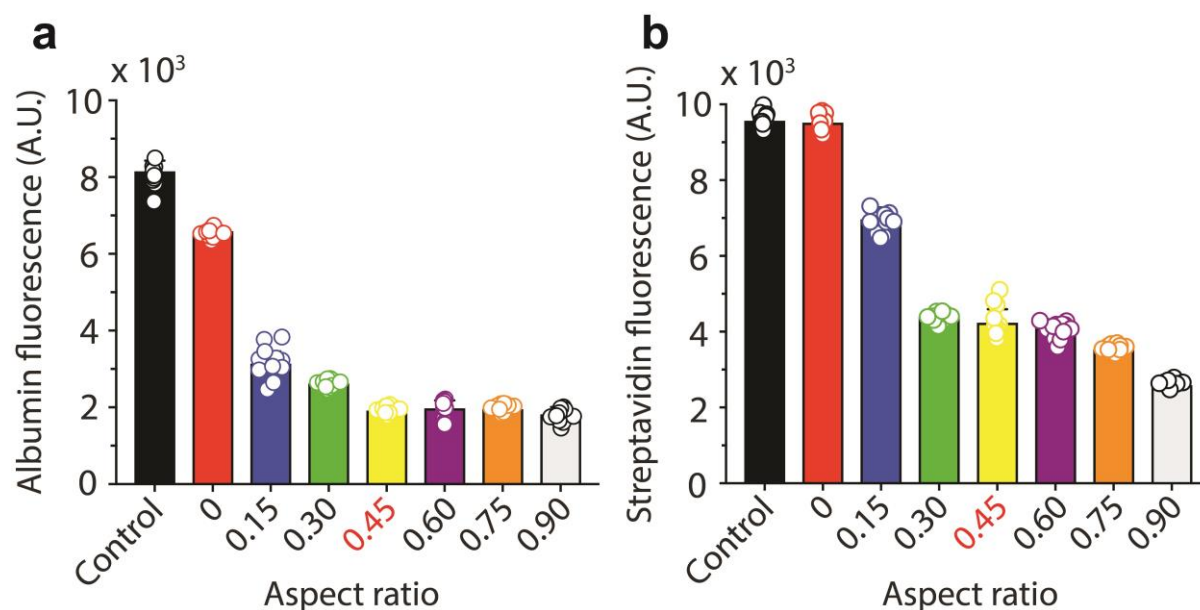




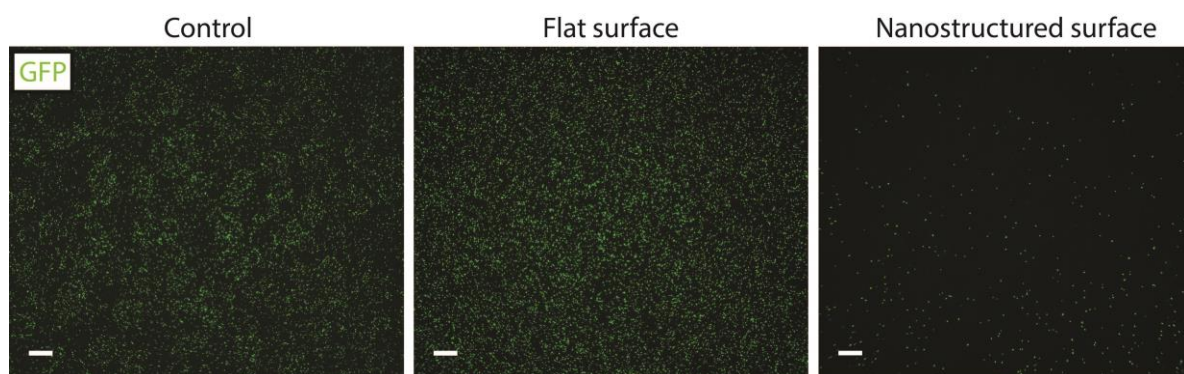
**Supplementary Figure S9 | Simulated transmission profile of the flat and nanostructured  $\text{Si}_3\text{N}_4$  membranes.** The simulated transmission profile of the **a**, flat and **b**, nanostructured  $\text{Si}_3\text{N}_4$  membranes are in good agreement with experimental transmittance measurements shown in Fig. 3. The nanostructured  $\text{Si}_3\text{N}_4$ -membrane shows significant reduction in the angle dependence.



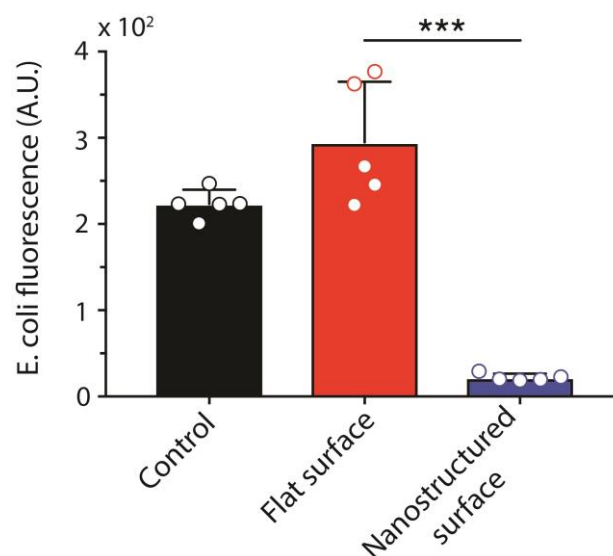
**Supplementary Figure S10 | Scattering effects of nanostructures on  $\text{Si}_3\text{N}_4$ -membrane.** By gradually increasing the aspect ratio (height) of the nanostructures from 0 (i.e. flat membrane) to 0.45 in a FEM simulator using the exact geometry of the fabricated samples, a gradual increase in the total transmission is observed.



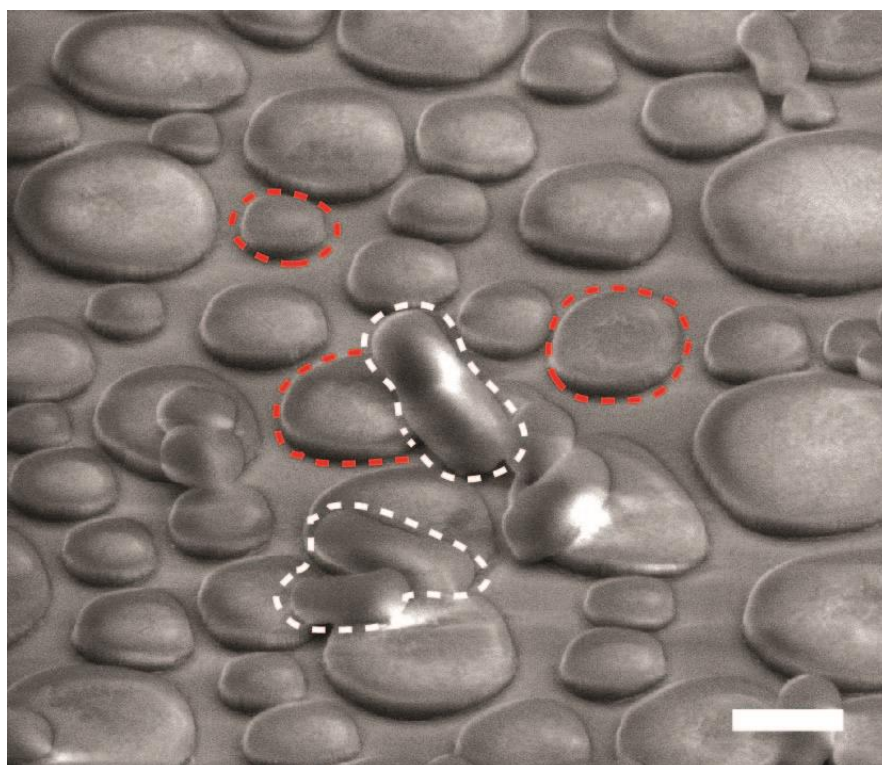
**Supplementary Figure S11 | Protein resistance of the nanostructured  $\text{Si}_3\text{N}_4$  templates.** The resistance against the adhesion of albumin and streptavidin was measured through intensity-based fluorescence microscopy ( $n = 12$  representative images). Nanostructured  $\text{Si}_3\text{N}_4$  templates with different aspect-ratios (0 – 0.90) were studied. In both cases, a sharp decline in protein adhesion was observed upon structuring the  $\text{Si}_3\text{N}_4$  (aspect-ratio  $\geq 0.15$ ). The protein adhesion on the flat  $\text{Si}_3\text{N}_4$  (aspect-ratio = 0) was comparable to that of the positive control. The aspect-ratio of 0.45 chosen for use with an IOP-sensing implant is highlighted in red. The experiment was conducted once. Error bars are given by the standard deviation about the mean.



**Supplementary Figure S12 | Bacterial resistance of the nanostructured  $\text{Si}_3\text{N}_4$  surface.** Fluorescent micrographs of positive control, flat  $\text{Si}_3\text{N}_4$ , and nanostructured  $\text{Si}_3\text{N}_4$  surfaces incubated for 4 hours in *E. coli* cultures transformed with green fluorescent protein (GFP)-expressing pFluoroGreen™ plasmid. Minimal bacterial adhesion is observed on the nanostructured  $\text{Si}_3\text{N}_4$  surface compared to the flat  $\text{Si}_3\text{N}_4$  and control surfaces. Scale bars, 100  $\mu\text{m}$ .

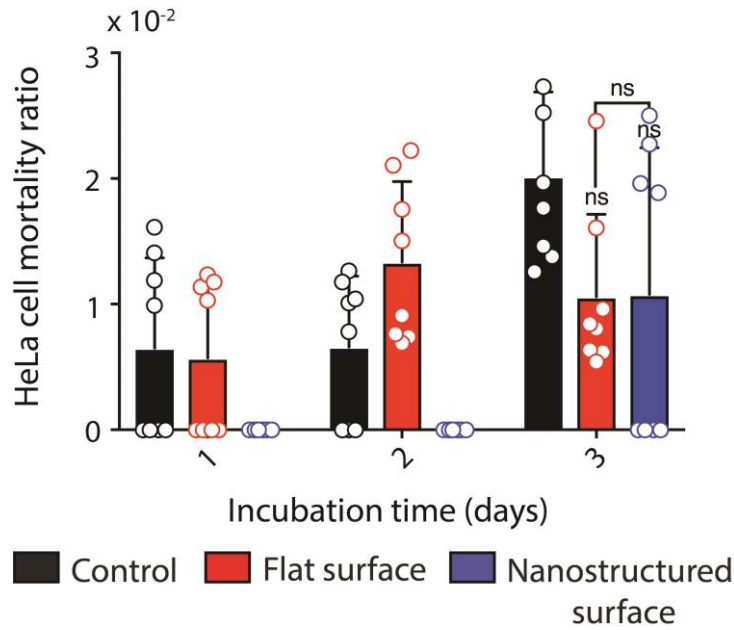


**Supplementary Figure S13 | Bacterial adhesion as a function of fluorescence intensity.** The average *E. coli* fluorescence intensity observed on the nanostructured  $\text{Si}_3\text{N}_4$  surface was considerably lower than the flat  $\text{Si}_3\text{N}_4$  surface ( $***P \leq 0.001$ , one-way ANOVA with post-hoc Tukey test, s.d.,  $n = 5$  representative images). Adjustments were made for multiple comparisons. The experiment was replicated two times. Error bars are given by the standard deviation about the mean.

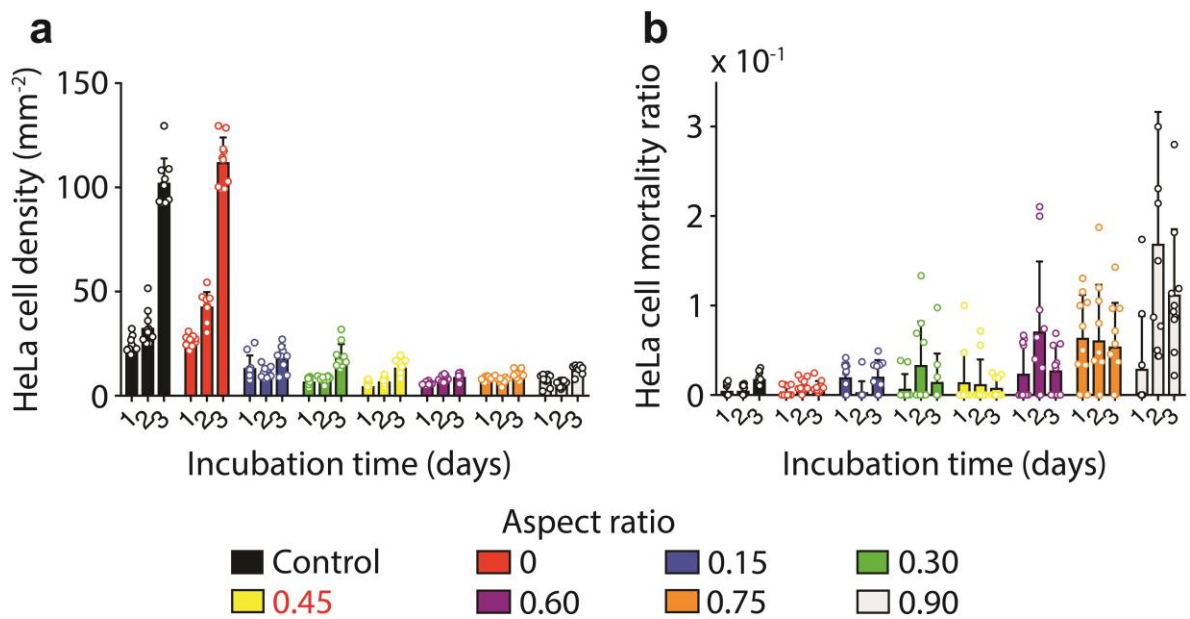


**Supplementary Figure S14 | SEM image of *E. coli* on the nanostructured  $\text{Si}_3\text{N}_4$  surface.** The

nanostructures (circled in red) do not disrupt the shape of the cells (circled in white) and therefore do not induce physical lysis as seen in high aspect-ratio structures. Here, antifouling is achieved through anti-adhesion. Scale 1  $\mu\text{m}$ .



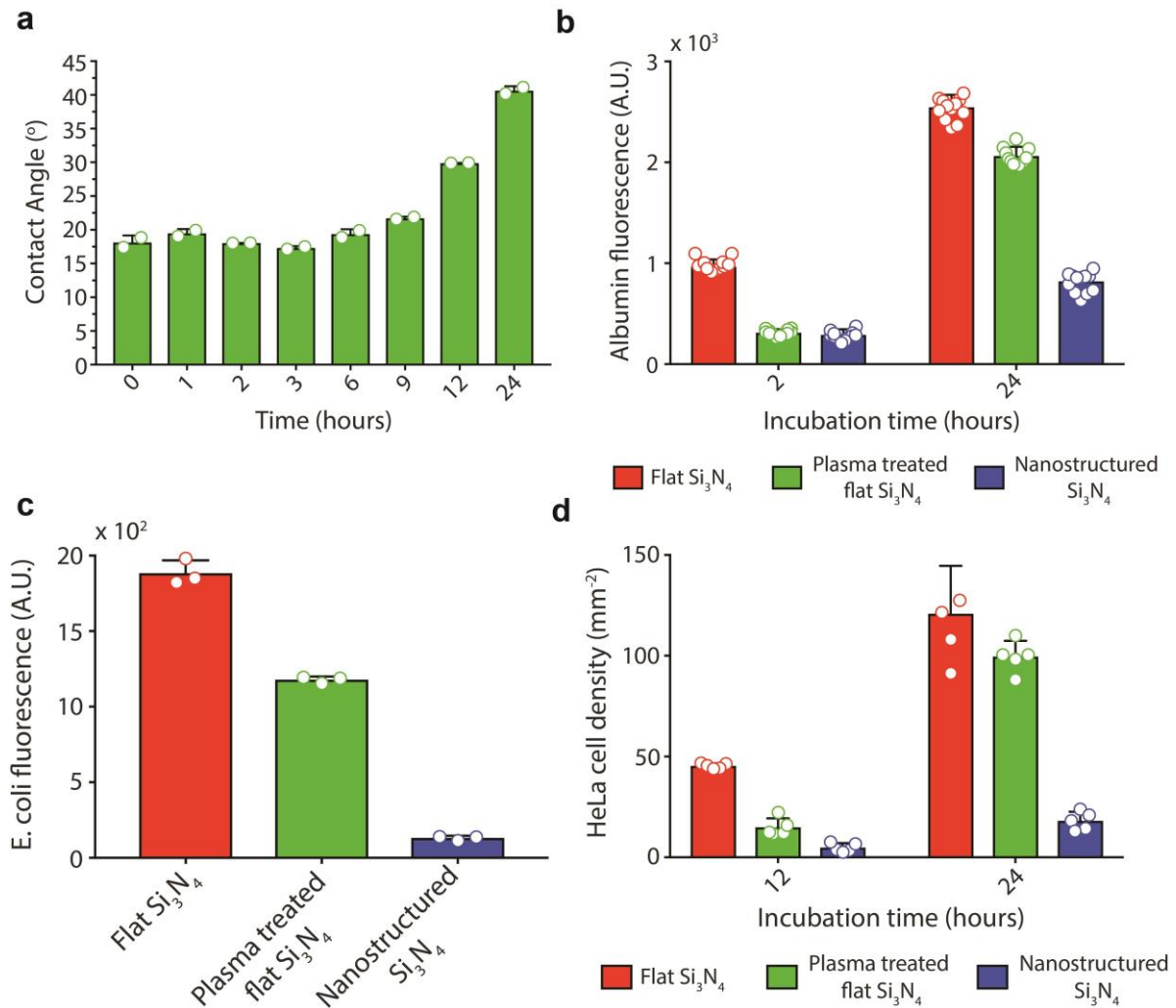
**Supplementary Figure S15 | HeLa cell mortality ratio.** Statistically similar mortality ratios (measured as the ratio of the number of dead cells to living cells) displayed by the control, flat  $\text{Si}_3\text{N}_4$ , and nanostructured  $\text{Si}_3\text{N}_4$  surfaces after 72 hours ( $P > 0.05$ , ns: not significant, two-way ANOVA with Bonferroni's multiple comparisons test, s.d.,  $n = 8$  representative images). Adjustments were made for multiple comparisons. The experiment was replicated two times. Error bars are given by the standard deviation about the mean.



**Supplementary Figure S16 | Biophysical interaction of nanostructured  $\text{Si}_3\text{N}_4$  template with HeLa cells.** **a**, HeLa live cell density was computed over 72 hours at 24-hour intervals using 10 representative fields-of-view captured through wide-field epifluorescence microscopy. A sharp

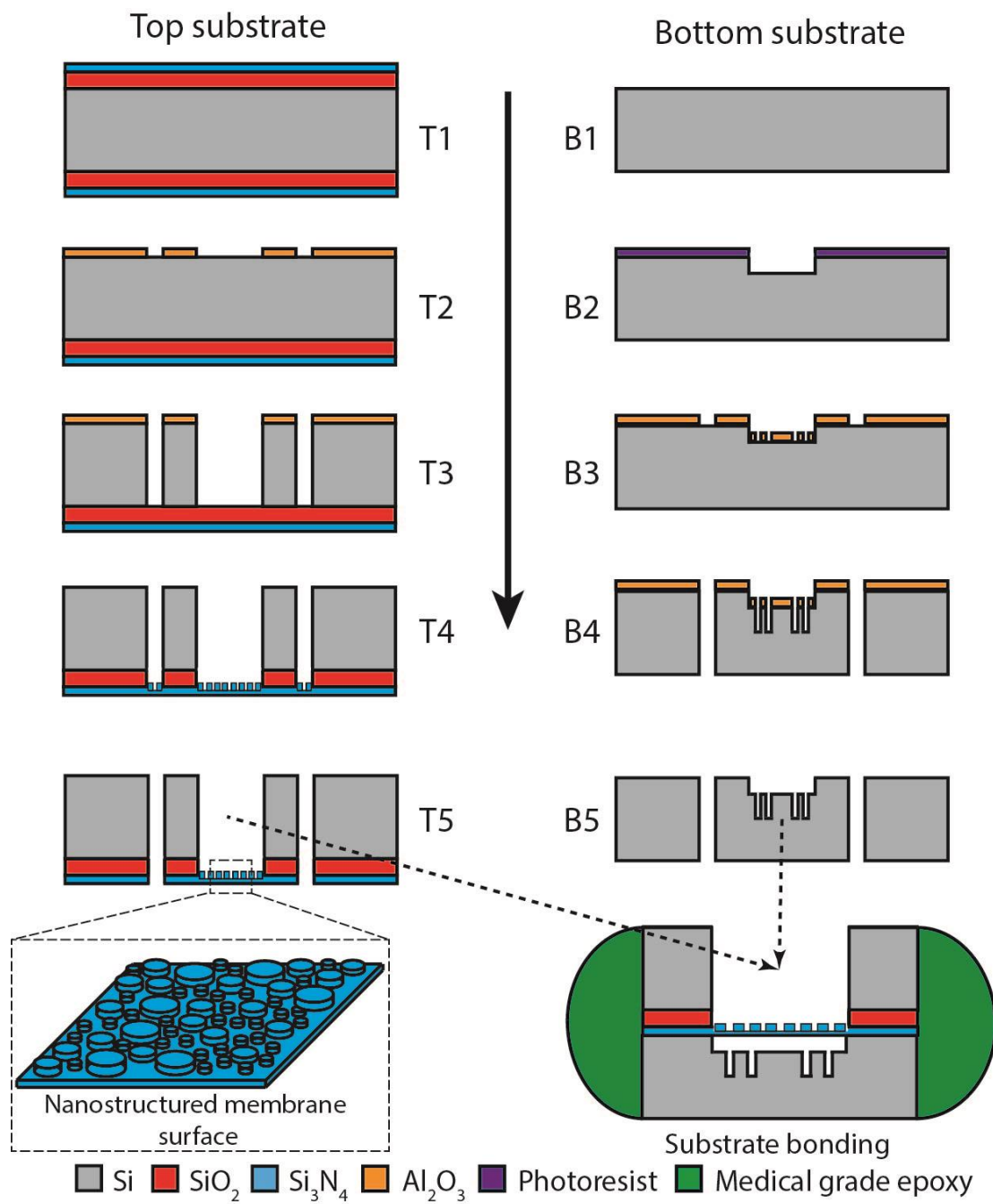


reduction in adherent live cell density was observed upon structuring  $\text{Si}_3\text{N}_4$  with nanostructures ( $n = 10$  representative images). **b**, HeLa cell viability was quantified as the ratio between the number of dead to living cells per field-of-view using 10 representative fields-of-view captured through wide-field epifluorescence microscopy ( $n = 10$  representative images). Higher rates of physically induced lyses were observed with increased nanostructured  $\text{Si}_3\text{N}_4$  aspect-ratios. The aspect-ratio of 0.45 chosen to implement the nanostructured  $\text{Si}_3\text{N}_4$ -membrane for the IOP-sensing implant is highlighted in red. The experiment was conducted once. Error bars are given by the standard deviation about the mean.

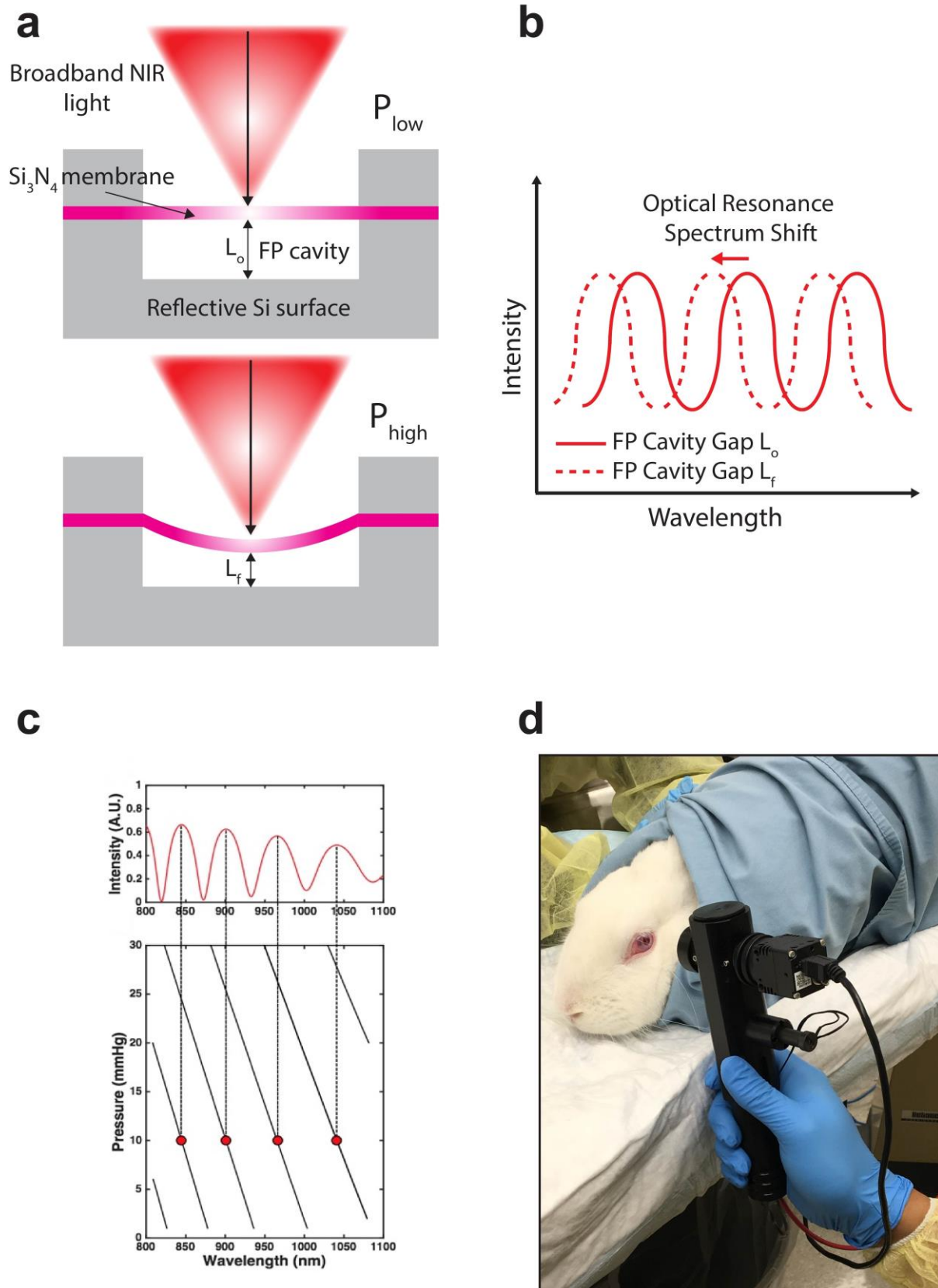


**Supplementary Figure | S17. Importance of nanoscale surface topology in anti-biofouling of the nanostructured  $\text{Si}_3\text{N}_4$  surface.** **a**, Contact angle vs. time elapsed after plasma treatment: flat  $\text{Si}_3\text{N}_4$  surfaces were plasma-oxidised in order to lower their contact angles to values comparable to the nanostructured  $\text{Si}_3\text{N}_4$  surface ( $n = 2$  measurements). Plasma oxidation produced non-permanent enhanced hydrophilicity that dissipates in 24 hours. **b**, Bovine serum albumin (BSA) adhesion measured as a function of fluorescence intensity on untreated flat, plasma treated flat  $\text{Si}_3\text{N}_4$  and nanostructured  $\text{Si}_3\text{N}_4$  surfaces: in case of protein anti-adhesion, hydrophilicity plays a greater role than the nanotopology of the nanostructures ( $n = 12$  representative images). **c**, *E. coli* adhesion measured as a function of fluorescence intensity after 4 hours of incubation ( $n = 3$  representative images). **d**, HeLa cell density measured after 12 hours and 24 hours ( $n = 5$  representative images). For cells, nanotopology plays a greater role as indicated by greater adhesion resistance offered by the nanostructured  $\text{Si}_3\text{N}_4$  surface over the plasma treated  $\text{Si}_3\text{N}_4$  surface of a similar contact angle. The experiment was conducted once. Error bars are given by the standard deviation about the

mean.

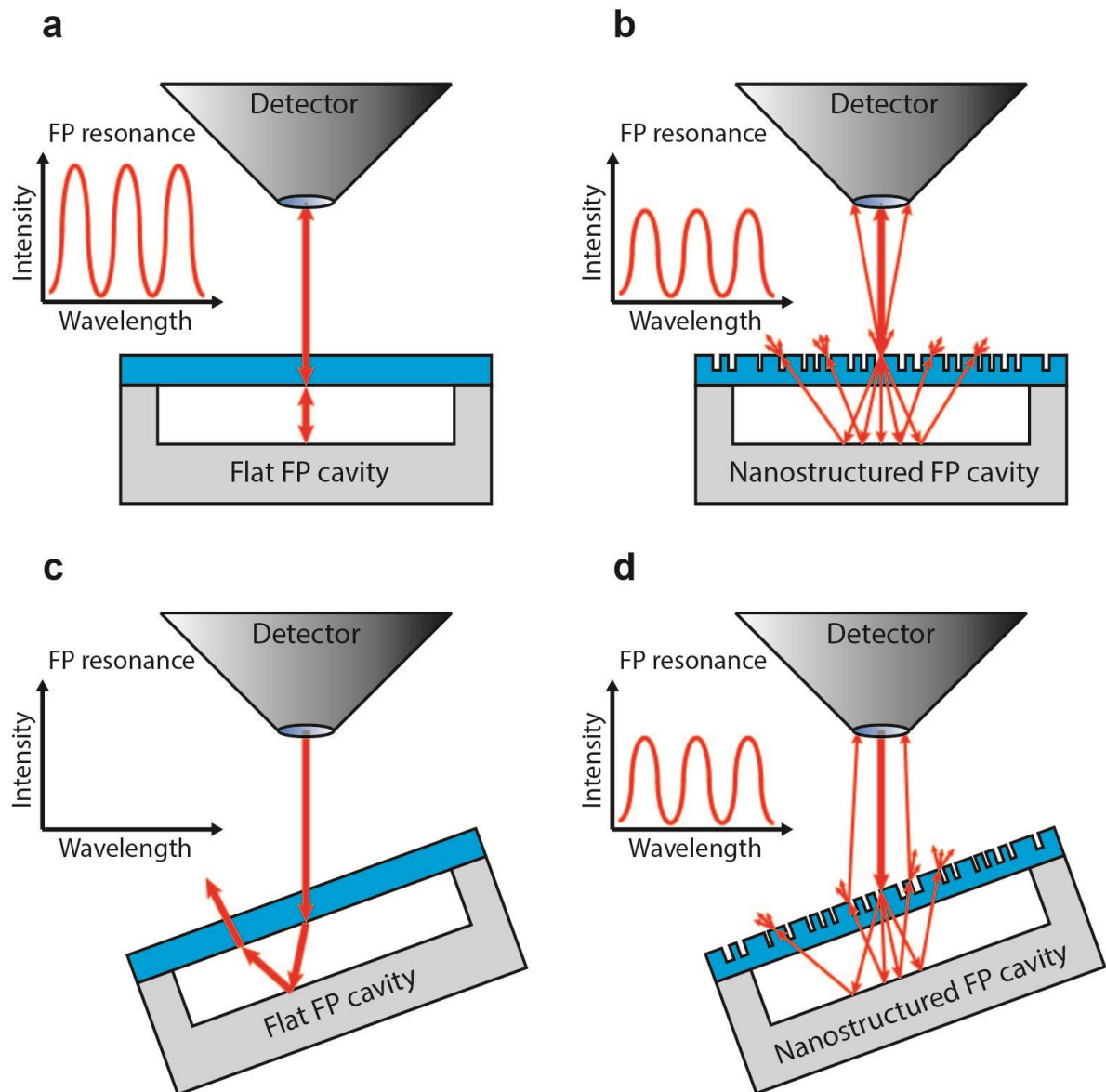


**Supplementary Figure S18 | Fabrication process flow of the nanostructured IOP sensor.**  
The top and bottom substrates are separately fabricated and later assembled together.



**Supplementary Figure S19 | IOP calculation from the sensor-reflected spectrum.** **a**, micro-optical IOP sensor implant schematic. The hermetically-sealed Fabry-Perot (FP) IOP sensor has two important surfaces: (1) a flexible deformable  $\text{Si}_3\text{N}_4$ -membrane serving as an optomechanical sensing element and forming the top surface of the FP-resonator; and (2) a reflective Si mirror-like surface that forms the bottom surface. The two surfaces are separated by a gap thereby forming an

FP cavity. If IOP increases, the  $\text{Si}_3\text{N}_4$ -membrane deflects inwards, decreasing the cavity gap size. **b**, The decrease in cavity gap size results in a blue-shift of the FP-cavity resonance spectrum which would be detected through reflection spectroscopy. **c**, A measured raw spectrum (top) and how its peaks map into the pre-characterization lines (bottom) generated in benchtop studies performed on the sensor before implantation. Each pre-characterization line represents the position of the associated peak as a function of pressure. The lines were generated by placing the sensor inside a pressure-controlled chamber connected with a reference digital pressure gauge and a pressure controller, and during a pressure ramp at a step size of 0.2 mmHg, the peak locations of each raw spectrum at a given pressure (provided by the digital pressure gauge) is recorded along with the pressure level. The relation between the given pressure and the associated set of the peak locations is one-to-one mapping. During *in vivo* studies, an IOP-identification algorithm maps the location of the major peaks in the raw spectrum reflected from the sensor to the best matching IOP-level using the pre-characterization lines. **d**, Custom-built hand-held detector interfaced with a CCD camera and a mini-spectrometer for live *in vivo* IOP detection in awake New Zealand white rabbits.



**Supplementary Figure S20 | Angle-dependent properties of the FP cavity and improvement using nanostructured  $\text{Si}_3\text{N}_4$ .** **a**, A flat-surfaced FP cavity under normal incidence provides a correct, high signal-to-noise ratio (SNR) reflection spectrum. **b**, In comparison, a nanostructured FP cavity produces a reflection spectrum of marginally reduced SNR due to optimally controlled



forward scattering. **c**, Under oblique incident angles, the interaction of light within the flat-surfaced FP cavity is purely specular and no reflected signal is acquired beyond the fixed numerical aperture (NA) of the detector objective. **d**, The reflection spectrum from the nanostructured FP cavity can still be detected at oblique incident angles owing to the forward scattering effect of the nanostructured membrane, thereby greatly expanding the sensor's range of the detection angles.